

Building Holographic Entanglement by Measurement

Jonathan Jeffrey,^{1,2} Lucien Gandarias,¹ Monika Schleier-Smith,¹ and Brian Swingle³

¹*Department of Physics, Stanford University, Stanford, California 94305, USA*

²*Department of Applied Physics, Stanford University, Stanford, California 94305, USA*

³*Department of Physics, Brandeis University, Waltham, Massachusetts 02453, USA*

(Dated: January 30, 2026)

We propose a framework for preparing quantum states with a holographic entanglement structure, in the sense that the entanglement entropies are governed by minimal surfaces in a chosen bulk geometry. We refer to such entropies as holographic because they obey a relation between entropies and bulk minimal surfaces, known as the Ryu-Takayanagi formula, that is a key feature of holographic models of quantum gravity. Typically in such models, the bulk geometry is determined by solving Einstein's equations. Here, we simply choose a bulk geometry, then discretize the geometry into a coupling graph comprising bulk and boundary nodes. Evolving under this graph of interactions and measuring the bulk nodes leaves behind the desired pure state on the boundary. We numerically demonstrate that the resulting entanglement properties approximately reproduce the predictions of the Ryu-Takayanagi formula in the chosen bulk geometry. We consider graphs associated with hyperbolic disk and wormhole geometries, but the approach is general. The minimal ingredients in our proposal involve only Gaussian operations and measurements and are readily implementable in photonic and cold-atom platforms.

At the largest length scales, gravity dominates, but at the smallest scales, the rules of quantum theory hold sway. Physicists have long searched for a more general framework that combines these two regimes, a theory of quantum gravity. Direct experimental access to quantum effects in gravity has not yet been achieved, so the study of quantum gravity is driven by a number of conceptual puzzles that arise when quantum field theory and general relativity are combined. For example, the realization that black holes are thermal objects with an entropy proportional to their area rather than their volume [1, 2] led to the idea that quantum gravity is fundamentally holographic, with the geometry of spacetime emerging from microscopic degrees of freedom living on a boundary of one dimension fewer [3, 4]. The best understood version of this holographic framework is known as the anti-de Sitter space / conformal field theory correspondence (AdS/CFT) [5–8]. This correspondence is a precise duality between a quantum system with no dynamical gravity (CFT) and a quantum gravitational system (AdS). The CFT is naturally defined at the boundary of the dual “bulk” asymptotically AdS spacetime.

Entanglement plays a central role in AdS/CFT and is closely related to the emergence of spacetime [9, 10]. The AdS/CFT dictionary relates states in the boundary to states in the bulk, which often correspond to smooth geometries. In such cases, the bulk geometry encodes the entanglement structure of the CFT as quantified by the Ryu-Takayanagi (RT) formula: the von Neumann entropies of subregions of the boundary CFT are equal to the areas of corresponding minimal surfaces in the bulk geometry, to leading order in Newton's constant [9]. This formula can be thought of as a vast generalization of the older formula for black hole entropy [1, 2], to which it reduces in special cases.

Holographic duality is less well understood outside of the small set of special quantum systems whose bulk duals correspond to some form of Einstein gravity in the semiclassical limit [8]. A core issue is that the boundary side is in general a strongly correlated system that is hard to analyze with conventional theoretical tools. Yet the boundary is potentially amenable to quantum simulation, as suggested by several theoretical proposals [11–18] and proof-of-principle experiments [19–25] aimed at simulating aspects of holographic duality in the lab. Still, preparing holographic boundary states for arbitrary bulk geometries remains an open challenge.

In this paper, we show how states with holographic patterns of entanglement can be prepared using programmable interactions and measurements in constant time. We focus on a Gaussian version of our protocol for its tractability, but we also discuss prospective generalizations. The key idea is illustrated in Figure 1: given a desired geometry, which is discretized into a graph, one first evolves an initially unentangled state with a simple quench Hamiltonian determined by the graph. One then measures the bulk part of the graph, leaving behind a pure state on the boundary. Our central result is that this boundary state has a holographic entanglement structure in that the entropies of boundary subregions are approximately equal to the predictions of the RT formula in the chosen geometry. Our framework provides both a theoretical laboratory for further investigation of holographic entanglement and an experimentally accessible method for engineering designer bulk geometries. In particular, photonic systems, atomic ensembles in cavities, or superconducting circuits can be used to implement our protocol with existing technology.

Our approach is partly inspired by tensor-network models of holographic duality [26–28] and measurement-

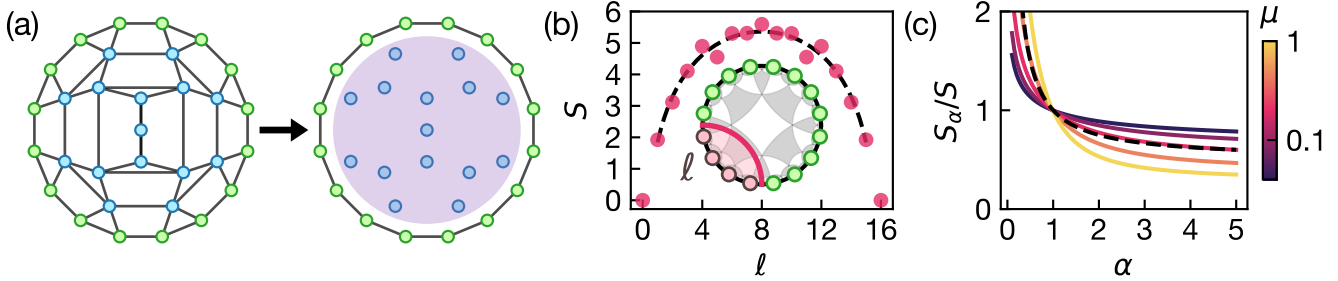


FIG. 1. (a) The quench-and-measure protocol. The input state is a set of independent squeezed Gaussian modes, with some designated as the bulk (blue circles) and others as the boundary (green circles). After quenching on interactions with a specified coupling graph (black lines), chosen here to discretize a hyperbolic disk, measurement of the bulk nodes prepares the boundary in a pure state. (b) Entanglement entropies S of connected boundary regions of length ℓ for initial squeezing parameter $\mu = 0.2$, compared with the fit to the prediction for a (1+1)D CFT on a circle (dashed black line), where the central charge $c = 6.5(3)$ and vertical offset $\epsilon = 5.36(8)$ are free parameters. Through the Ryu-Takayanagi formula, the entanglement entropy S has a geometrical interpretation as proportional to the minimal length in a holographic bulk (inset schematic). (c) Rényi entropy (normalized by entanglement entropy) vs index α for a region size $\ell = 4$ on the boundary and various squeezing parameters μ (colored lines), compared to the CFT prediction (dashed black line).

based protocols for preparing entangled states [17, 29, 30]. We have focused on the RT formula as the primary characteristic of holographic entanglement, but a full holographic dual has additional properties. These include Rényi entropies which depend non-trivially on the Rényi index and power-law correlations for some observables. Many existing toy models of holographic entanglement are unable to capture these additional features, for example, tensor network models based on stabilizer states [27], as well as random tensor networks [28], have Rényi entropies that are independent of the Rényi index and no power-law correlations. Since these early examples, a wide variety of tensor network and holographic code models have been developed, some of which also have power-law correlations [31–44]. Our states turn out to automatically have Rényi entropies that vary with the Rényi index and, for suitably designed graphs, we also obtain clean power laws in certain correlation functions.

Quench-and-Measure Protocol—We consider a collection of N sites, each of which is host to a single position degree of freedom x_i with an associated canonical momentum p_i . These quadrature operators obey the standard commutation relations, $[x_i, p_j] = i\delta_{ij}$, for $i, j \in \{1, \dots, N\}$. It will be convenient to group these quadrature operators into a phase space vector, $\xi = (x_1, \dots, x_N, p_1, \dots, p_N)$. For later use, we also divide these degrees of freedom into two sets, boundary (bdy) and bulk (bulk).

The system is initialized into an unentangled Gaussian state of the form

$$\psi_0(x) \propto \prod_i e^{-\frac{\mu}{2}x_i^2}. \quad (1)$$

Here, $\mu = 1$ represents the case where each oscillator is initialized in the vacuum state, and more generally $\mu \neq 1$

allows for initial squeezing in each mode. Starting from this initial state, we quench the system by evolving for a time t with the Hamiltonian

$$H_q = \frac{1}{2} \sum_{i,j} J_{ij} x_i x_j, \quad (2)$$

where J is a coupling matrix between the oscillators. J must be real and symmetric, and in the simplest case it will be the adjacency matrix of an unweighted graph. For strong initial squeezing $\mu \ll 1$ (or long time t), the resulting entangled state is then a continuous-variable graph state [45], and its entropies are closely related to those of “perfect tensors” [46]. More generally, the entanglement depends only on the combination t/μ , so below we will fix the quench time to $t = 1$.

Following the quench, we measure all the bulk sites in the momentum basis. Based on the measurement outcomes, we may optionally apply local phase space displacements to the unmeasured boundary sites to obtain a state in which $\langle x_i \rangle = \langle p_i \rangle = 0$ for all $i \in \text{bdy}$. The resulting state is a pure state of the boundary degrees of freedom that does not depend on the measurement outcome. We will investigate the entanglement structure of the resulting boundary state for different choices of the coupling matrix J and initial squeezing μ .

The entanglement between the modes of the Gaussian state can be determined from the covariance matrix $\mathcal{V} = \langle \xi \xi^T \rangle - \langle \xi \rangle \langle \xi \rangle^T$, with elements $\mathcal{V}_{ij} = \text{Cov}(\xi_i, \xi_j) = \langle \{\xi_i - \langle \xi_i \rangle, \xi_j - \langle \xi_j \rangle\} \rangle$ [47–50]. We thus focus on how the covariance matrix transforms under the quench and under measurements. For initial squeezing μ , the initial covariance matrix is

$$\mathcal{V}_0 = \begin{pmatrix} \mathcal{V}_{0,x} & 0 \\ 0 & \mathcal{V}_{0,p} \end{pmatrix} = \begin{pmatrix} \frac{1}{2\mu} I & 0 \\ 0 & \frac{\mu}{2} I \end{pmatrix} \quad (3)$$

where I is the identity matrix. Solving the Heisenberg equation of motion $d\xi/dt = i[H_q, \xi]$ for the evolution under the quench shows that the operators undergo a symplectic transformation $\xi(t) = \mathcal{S}(t)\xi(0)$ given by

$$\mathcal{S}(t) = \begin{pmatrix} I & 0 \\ -Jt & I \end{pmatrix}. \quad (4)$$

The resulting covariance matrix after the quench is

$$\mathcal{V}_{\text{quenched}} = \mathcal{S}\mathcal{V}_0\mathcal{S}^T = \frac{1}{2\mu} \begin{pmatrix} I & -Jt \\ -Jt & \mu^2 I + J^2 t^2 \end{pmatrix}. \quad (5)$$

We now wish to determine the state of the boundary conditioned on a measurement of the bulk. To this end, we reorder the overall covariance matrix as

$$\mathcal{V} = \begin{pmatrix} \mathcal{V}_{\text{bdy}} & \mathcal{C} \\ \mathcal{C}^T & \mathcal{V}_{\text{bulk}} \end{pmatrix}, \quad (6)$$

where \mathcal{V}_{bdy} and $\mathcal{V}_{\text{bulk}}$ are covariance matrices of the boundary and bulk, respectively, and \mathcal{C} quantifies the bulk-boundary correlations. The conditional covariance matrix after a partial homodyne measurement in the momentum basis on this state can be calculated as

$$\mathcal{V}_{\text{bdy}|\text{bulk}} = \mathcal{V}_{\text{bdy}} - \mathcal{C}(\Pi_p \mathcal{V}_{\text{bulk}} \Pi_p)^{\text{MP}} \mathcal{C}^T \quad (7)$$

where MP is the Moore-Penrose inverse and Π_p is the projection matrix onto momentum for the bulk subsystem.

The conditional covariance matrix $\mathcal{V}_{\text{bdy}|\text{bulk}}$ is independent of the measurement outcomes, with each instance of the protocol preparing a quantum state that is equivalent up to local displacements. In particular, the conditional mean values $\langle \xi \rangle_{\text{bdy}|\text{bulk}}$ of the boundary depend on the bulk measurement outcomes ξ_{bulk} as $\langle \xi \rangle_{\text{bdy}|\text{bulk}} = \mathcal{C}(\Pi_p \mathcal{V}_{\text{bulk}} \Pi_p)^{\text{MP}} \xi_{\text{bulk}}$ [51]. To make the protocol fully deterministic, one may apply a final feedback step consisting of local displacements that shift these post-measurement means to zero.

Example Geometries—To illustrate the quench-and-measure protocol, we first consider a quench with J being the adjacency matrix of a graph G whose vertices are the sites. Based on two examples, a hyperbolic disk and a wormhole, we show numerically that the entanglement entropies are well fit by the RT formula in the corresponding geometry.

Consider the graph shown in Figure 1 inspired by the MERA tensor network [52] and discretizations of the hyperbolic disk. Within AdS/CFT, such a geometry would be associated to the ground state of the boundary CFT, so we compare the numerical entanglement to ground-state CFT predictions. For any CFT defined in one spatial dimension, the entanglement of a subregion of angle $\Delta\theta$ in the ground state on a circle is

$$S_{\text{gs}}(\Delta\theta) = \frac{c}{3} \ln \left(\sin \frac{\Delta\theta}{2} \right) + \epsilon, \quad (8)$$

where c is the central charge and ϵ is a non-universal constant related to the UV cutoff [53]. Note that $S_{\text{gs}}(2\pi - \Delta\theta) = S_{\text{gs}}(\Delta\theta)$ as required for a translation-invariant pure state. The RT formula applied to AdS_3 predicts the same form (reviewed in Supplemental Material [50]).

Figure 1(b) compares the numerically obtained entanglement (pink dots) with a fit to the CFT prediction (black dashed line), where c and ϵ are free parameters. The CFT prediction captures well the overall shape of the data, with only small deviations due to lattice artifacts. The fit value of c scales with $\ln \frac{1}{\mu}$ when μ is small, and the shape of the entropy curve depends to some extent on the magnitude of μ (see Supplemental Material [50]).

Full-featured holographic duals also have Rényi entropies with non-trivial dependence on the Rényi parameter. The Rényi entropy of a density matrix ρ is defined as $S_\alpha(\rho) = \frac{1}{1-\alpha} \ln \text{tr}(\rho^\alpha)$, and it can also be computed from the covariance matrix [50]. For our setting with the disk graph, the results are shown in Figure 1(c) for different values of the squeezing μ (colored curves). We see a non-trivial dependence on the Rényi parameter, in contrast to simple tensor-network models, and by tuning the squeezing we can come close to the CFT result $(S_\alpha/S)^{\text{CFT}} = (1 + 1/\alpha)/2$ (black dashed line) [54].

To demonstrate the power of the framework beyond the hyperbolic disk case, we also consider a wormhole geometry in which we take two copies of the graph for the hyperbolic disk, remove identical regions of the interior of each graph, and then glue the graphs together by adding corresponding links in the adjacency matrix. The resulting graph is shown in Figure 2(a). This wormhole geometry mimics a spatial slice of an eternal AdS black hole, and would be dual to the thermofield double state under AdS/CFT [55]. We consider the entanglement entropy for two different types of regions: either an interval on one side of the wormhole [Fig. 2(b)] or a pair of corresponding intervals on both sides [Fig. 2(c)].

For both the one-sided and two-sided regions, the entanglement entropy is well fit by minimal curves obtained from the (2+1)D eternal AdS black hole geometry [56] (see Supplemental Material for a review of the relevant geodesics [50]). In both cases, there is a competition between two different candidate minimal surfaces, shown in red and blue on the wormhole schematics in Fig. 2(b-c). The RT formula predicts a sharp change in the entanglement entropy when these two candidates swap dominance, and the calculated entanglement entropy (pink circles) shows a corresponding rapid crossover from one candidate to another (red and blue fit curves).

Power laws from decoration—These two examples of the quench-and-measure protocol yield states with entanglement entropies that are well approximated by minimal curves in a hyperbolic disk and wormhole geometry. They also have non-trivial Rényi entropies which can match CFT predictions. To also realize clean power-law correlations, it is useful to introduce an additional

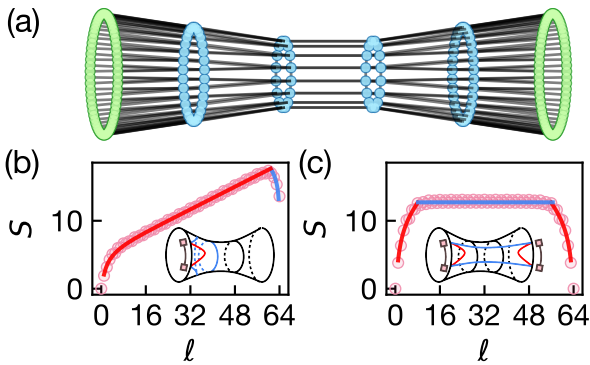


FIG. 2. (a) A wormhole graph, formed from gluing together portions of two hyperbolic disk graphs. In this case, each boundary has $L = 64$ sites. (b) One-sided entanglement entropy of the wormhole for $\mu = 0.2$, with the fit yielding inverse temperature $\beta = 2.9(1) \times 10^1$, central charge $c = 5.8(2)$, and offset $\epsilon = 2.1(1)$. The fit is shown in red and blue, which correspond to two different candidate curves for the minimal surface (see inset). (c) Two-sided entanglement entropy of the wormhole for $\mu = 0.2$. The approximate condition used to find the crossover between the red and blue candidate two-sided entanglement entropies for the model curve is given in [50].

structure to the quench Hamiltonian which we refer to as decoration. An example of a decorated graph is illustrated in Figure 3(a). It is constructed by first choosing a bulk graph (blue nodes) and choosing which bulk nodes are adjacent to boundary nodes (green nodes). The edges of the bulk graph are then split into two by adding intervening bulk nodes (yellow nodes). For each pair of split edges, one is assigned $+1$ in the J matrix defining the quench Hamiltonian and the other is assigned -1 .

The decoration procedure can be motivated by considering just three modes, labeled 1, 2, and 3. If all modes are initialized in an unentangled state, quenched with a $J_{12}x_1x_2 + J_{23}x_2x_3$ interaction, and mode 2 is subject to a momentum measurement, then the resulting correlations $\langle x_1x_3 \rangle$ have a sign given by $-\text{sgn}(J_{12}J_{23})$. Hence, if J_{12} and J_{23} have opposite signs, then the resulting post-measurement correlation is positive. The split nodes in the decorated graph thus ensure a non-alternating pattern of correlations [50].

As an example, we consider the decorated graph in Fig. 3, derived from the hyperbolic disk graph in Fig. 1. We examine the state prepared by the quench-and-measure protocol on this graph for strong initial squeezing, $\mu = 0.05$. In this regime, both the CFT ground-state entanglement entropy formula and power-law decay for the position-position two-point function are approximately satisfied, the latter exhibiting a scaling dimension of $\Delta_x \approx 1$. The scaling dimension of an operator ϕ is extracted from covariance by the relationship $\text{Cov}(\phi_i, \phi_j) \propto \sin(\pi|i-j|/L)^{-2\Delta_\phi}$. In this strong squeezing regime, the momentum-momentum correlations are

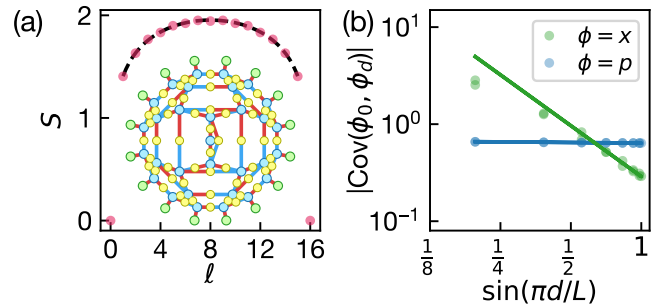


FIG. 3. (a) Entanglement entropies for the boundary of a depth-5 decorated graph for $\mu = 0.05$, along with the CFT fit (dashed black line) yielding $c = 1.004(9)$ and vertical offset $\epsilon = 1.954(2)$. The inset shows the decorated graph, where green are boundary nodes, blue are the original bulk nodes, and yellow are additional bulk nodes. The color of the edge indicates the sign of the interaction (red for positive, blue for negative). (b) Position (green) and momentum (blue) covariances of a pair of boundary sites vs distance d , where the boundary circumference is $L = 16$. Lines show power-law fits at large $\sin(\pi d/L)$, yielding scaling dimensions $\Delta_x = 0.87(4)$ and $\Delta_p = 1.03(3) \times 10^{-2}$.

approximately constant with distance, corresponding to a scaling dimension $\Delta_p \approx 0$. The central charge fit to the CFT entanglement entropy saturates at $c = 1$ (see Supplemental Material [50]), which is the same as for a (1+1)D free boson CFT. Based on these similarities, it will be interesting to understand if the decorated construction provides a lattice regularization of the free boson ground state.

Bulk reconstruction—Having demonstrated entropy results consistent with the RT formula in a variety of examples, a natural next question is whether the putative RT surface can be directly detected. To study this, we consider a problem of “bulk reconstruction” defined as follows. Consider, for example, the undecorated protocol for a graph G . Choose any bulk site and modify the graph by adding one boundary site which connects to the chosen bulk site. We refer to this new boundary site as the probe and emphasize that, although it connects directly to the bulk, it is not measured. Measure the bulk sites as before to construct a pure boundary state, now including the additional probe site. The physics of the probe is conveniently discussed in terms of the mutual information, $I(A : B) \equiv S(A) + S(B) - S(A \cup B)$. Because the probe is entangled with the rest of the boundary and the total state is pure, the mutual information between the probe b and the rest of the boundary is

$$I(\text{bdy} : b) = 2S(b). \quad (9)$$

More generally, if A is a subset of the rest of the boundary, then the entanglement with the probe can be recovered just from A if the mutual information satisfies $I(A : b) = 2S(b)$ [57].

By fixing a boundary subset A and varying the location of the probe, we can use the normalized mutual information, $I(A : b)/S(b)$, to map out the degree to which a bulk site can be reconstructed from the given boundary region. The connection to the RT surface arises because, in a holographic system obeying the RT formula, one can show that the normalized mutual information is 2 when the probe is connected to a bulk site inside the RT surface of the given boundary region and zero when it is connected to a bulk site outside. Hence, the boundary between the reconstructible and non-reconstructible regions, defined as $I(A : b)/S(b) > 1$ and < 1 respectively, should track the RT surface.

As a proof of principle, we demonstrate this diagnostic in the MERA/hyperbolic disk case. The four panels in Figure 4 show different boundary regions: a single interval (top) or a pair of intervals of different sizes (bottom). The pink highlighted boundary sites indicate the boundary region of interest, with the other boundary sites being green. The bulk sites are then colored ranging from pink to black indicating the size of the corresponding normalized mutual information. The dark pink solid line in the bulk indicates the RT prediction, in this case segments of circles on the Poincaré disk model of hyperbolic space. We see reasonably good agreement with the holographic prediction, with bulk sites deep inside the RT surface having high mutual information and bulk sites far outside having very low mutual information. However, the boundary is not completely sharp, suggesting a thickening or fluctuation of the RT surface that merits future investigation.

Outlook—We introduced a Gaussian quench-and-measure protocol and gave ample numerical evidence that it prepares states with holographic entanglement dictated by a bulk geometry of our choice. Our approach is inspired by tensor network models, and it naturally includes additional features such as non-trivial Rényi entropies and the possibility of power-law correlations. As the states output by our protocol are Gaussian, their entanglement properties can be efficiently reconstructed from measured correlations [58]. Moreover, by leveraging measurement rather than relying on dynamical spreading of correlations, the protocol generates long-range entanglement in $O(1)$ quench time. Hence, our proposal provides an efficient framework to prepare and probe holographic states and can serve as a starting point for generalizations.

Our proposal is amenable to instantiation on several experimental platforms. At the heart of our protocol is the quench that prepares a continuous-variable graph state. Such states have been generated in photonic platforms [59–61] and in arrays of atomic ensembles with photon-mediated interactions [22, 62], both providing flexible control over the graph. A further possibility is to leverage superconducting circuits featuring hyperbolic lattices of coplanar waveguide resonators [63]. Our pro-

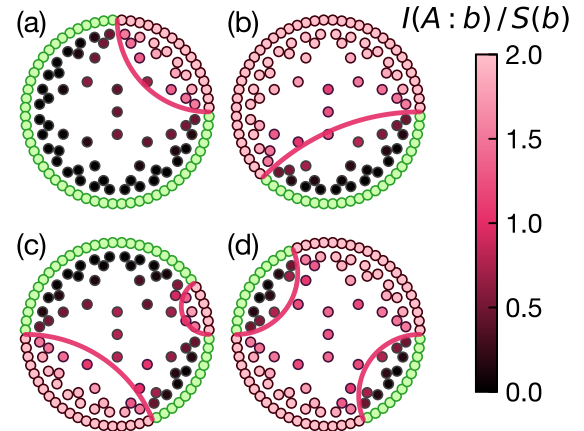


FIG. 4. Approximate reconstruction of the entanglement wedge through mutual information. The color of each bulk node shows the normalized mutual information $I(A : b)/S(b)$ between a subset of boundary nodes (light pink nodes on the ring) and an unmeasured probe b connected to the bulk node. Note that $2S(b)$ bounds $I(A : b)$. This undecorated construction uses $\mu = 1$, which leads to a sharper surface compared to stronger initial squeezing. The expected minimal surface is drawn in dark pink. The boundary regions R are (a) a small connected region (b) a large connected region (c) two disconnected regions with an expected disconnected entanglement wedge, and (d) two disconnected regions with an expected connected entanglement wedge.

tocol should also generalize to stabilizer states of qubits, opening the door to implementation in quantum computing platforms including reconfigurable arrays of Rydberg atoms [64] or trapped ions [65, 66].

Beyond their fundamental interest, the long-range entangled states generated by our protocol may serve as resources for sensing or computation. The scale-invariant correlations in the Gaussian setting could enable entanglement-enhanced imaging of spatially structured fields. Generalizations to stabilizer states of qubits, or incorporation of non-Gaussianity, may enable novel error correcting codes [67] and bring in new features of holography [68]. An important question for future work is whether our protocol can accommodate a degree of non-Gaussianity while keeping post-selection manageable. Future work may explore how experimental imperfections impact the state preparation and to what extent entanglement in such imperfectly prepared states can be described by a quantum extremal surface formula [69].

Our protocol also raises broader questions for future theoretical work benefiting from the tractability of the Gaussian setting. Prospects include seeking a deeper analytical understanding of the entanglement structure, a study of entropy inequalities and the entropy cone [70], perturbations and the problem of metric reconstruction [71], probes of complexity [72], and connections between wormholes and random Gaussian states [73].

We thank Eugene Demler, Soonwon Choi, Nadie Li,

Brian Khor, Allison Powell, Merrick Ho, and Ocean Zhou for discussions. We gratefully acknowledge support from the Heising-Simons Foundation under grants 2024-4849 (B.S.) and 2024-4850 (J. J. and M.S.-S.), the National Science Foundation under award number 2409479 (M. S.-S.), and the DOE Office of Science, Office of High Energy Physics under award DE-SC0025934 (L. G.).

[1] J. D. Bekenstein, Black holes and entropy, *Physical Review D* **7**, 2333 (1973).

[2] S. W. Hawking, Black hole explosions?, *Nature* **248**, 30 (1974).

[3] L. Susskind, The World as a hologram, *Journal of Mathematical Physics* **36**, 6377 (1995), arXiv:hep-th/9409089.

[4] G. 't Hooft, Dimensional reduction in quantum gravity (1993), arXiv:gr-qc/9310026 [gr-qc].

[5] J. M. Maldacena, The Large N limit of superconformal field theories and supergravity, *Advances in Theoretical and Mathematical Physics* **2**, 231 (1998), arXiv:hep-th/9711200.

[6] E. Witten, Anti-de Sitter space and holography, *Advances in Theoretical and Mathematical Physics* **2**, 253 (1998), arXiv:hep-th/9802150.

[7] S. S. Gubser, I. R. Klebanov, and A. M. Polyakov, Gauge theory correlators from noncritical string theory, *Physics Letters B* **428**, 105 (1998), arXiv:hep-th/9802109.

[8] O. Aharony, S. S. Gubser, J. M. Maldacena, H. Ooguri, and Y. Oz, Large N field theories, string theory and gravity, *Physics Reports* **323**, 183 (2000), arXiv:hep-th/9905111.

[9] S. Ryu and T. Takayanagi, Holographic Derivation of Entanglement Entropy from AdS/CFT, *Physical Review Letters* **96**, 181602 (2006), arXiv:hep-th/0603001.

[10] M. Van Raamsdonk, Building up spacetime with quantum entanglement, *General Relativity and Gravitation* **42**, 2323 (2010), arXiv:1005.3035 [hep-th].

[11] B. Swingle, G. Bentsen, M. Schleier-Smith, and P. Hayden, Measuring the scrambling of quantum information, *Physical Review A* **94**, 040302 (2016).

[12] D. Pikulin and M. Franz, Black hole on a chip: Proposal for a physical realization of the Sachdev-Ye-Kitaev model in a solid-state system, *Physical Review X* **7**, 031006 (2017).

[13] G. Bentsen, T. Hashizume, A. S. Buyskikh, E. J. Davis, A. J. Daley, S. S. Gubser, and M. Schleier-Smith, Treelike interactions and fast scrambling with cold atoms, *Physical Review Letters* **123**, 130601 (2019).

[14] B. Yoshida and N. Y. Yao, Disentangling scrambling and decoherence via quantum teleportation, *Physical Review X* **9**, 011006 (2019).

[15] A. R. Brown, H. Gharibyan, S. Leichenauer, H. W. Lin, S. Nezami, G. Salton, L. Susskind, B. Swingle, and M. Walter, Quantum gravity in the lab. I. teleportation by size and traversable wormholes, *PRX Quantum* **4**, 010320 (2023).

[16] S. Dey, A. Chen, P. Basteiro, A. Fritzsche, M. Greiter, M. Kaminski, P. M. Lenggenhager, R. Meyer, R. Sorbello, A. Stegmaier, *et al.*, Simulating holographic conformal field theories on hyperbolic lattices, *Physical Review Letters* **133**, 061603 (2024).

[17] A. Cowsik, M. Ippoliti, and X.-L. Qi, Engineering entanglement geometry via spacetime-modulated measurements, *Physical Review D* **112**, L081904 (2025).

[18] R. Sahay, M. D. Lukin, and J. Cotler, Emergent holographic forces from tensor networks and criticality, *Physical Review X* **15**, 021078 (2025).

[19] K. Li, M. Han, D. Qu, Z. Huang, G. Long, Y. Wan, D. Lu, B. Zeng, and R. Laflamme, Measuring holographic entanglement entropy on a quantum simulator, *npj Quantum Information* **5**, 30 (2019).

[20] K. A. Landsman, C. Figgatt, T. Schuster, N. M. Linke, B. Yoshida, N. Y. Yao, and C. Monroe, Verified quantum information scrambling, *Nature* **567**, 61 (2019).

[21] M. S. Blok, V. V. Ramasesh, T. Schuster, K. O'Brien, J.-M. Kreikebaum, D. Dahmen, A. Morvan, B. Yoshida, N. Y. Yao, and I. Siddiqi, Quantum information scrambling on a superconducting qutrit processor, *Physical Review X* **11**, 021010 (2021).

[22] A. Periwal, E. S. Cooper, P. Kunkel, J. F. Wienand, E. J. Davis, and M. Schleier-Smith, Programmable interactions and emergent geometry in an array of atom clouds, *Nature* **600**, 630 (2021).

[23] D. Jafferis, A. Zlokapa, J. D. Lykken, D. K. Kolchmeyer, S. I. Davis, N. Lauk, H. Neven, and M. Spiropulu, Traversable wormhole dynamics on a quantum processor, *Nature* **612**, 51 (2022), [Erratum: *Nature* 640, E32 (2025)].

[24] I. Shapoval, V. P. Su, W. d. Jong, M. Urbanek, and B. Swingle, Towards Quantum Gravity in the Lab on Quantum Processors, *Quantum* **7**, 1138 (2023).

[25] E. Granet, Y. Kikuchi, H. Dreyer, and E. Rinaldi, Simulating sparse SYK model with a randomized algorithm on a trapped-ion quantum computer (2025), arXiv:2507.07530 [quant-ph].

[26] B. Swingle, Entanglement renormalization and holography, *Physical Review D* **86**, 065007 (2012).

[27] F. Pastawski, B. Yoshida, D. Harlow, and J. Preskill, Holographic quantum error-correcting codes: Toy models for the bulk/boundary correspondence, *Journal of High Energy Physics* **2015**, 149 (2015), arXiv:1503.06237 [hep-th].

[28] P. Hayden, S. Nezami, X.-L. Qi, N. Thomas, M. Walter, and Z. Yang, Holographic duality from random tensor networks, *Journal of High Energy Physics* **2016**, 009 (2016), arXiv:1601.01694 [hep-th].

[29] H. J. Briegel and R. Raussendorf, Persistent entanglement in arrays of interacting particles, *Physical Review Letters* **86**, 910 (2001).

[30] N. Tantivasadakarn, R. Thorngren, A. Vishwanath, and R. Verresen, Long-range entanglement from measuring symmetry-protected topological phases, *Physical Review X* **14**, 021040 (2024).

[31] J. I. Latorre and G. Sierra, Holographic codes (2015), arXiv:1502.06618 [quant-ph].

[32] A. Bhattacharyya, Z.-S. Gao, L.-Y. Hung, and S.-N. Liu, Exploring the tensor networks/AdS correspondence, *Journal of High Energy Physics* **2016**, 10.1007/jhep08(2016)086 (2016).

[33] W. Donnelly, D. Marolf, B. Michel, and J. Wien, Living on the edge: a toy model for holographic reconstruction of algebras with centers, *Journal of High Energy Physics* **2017**, 10.1007/jhep04(2017)093 (2017).

[34] M. Han and S. Huang, Discrete gravity on random tensor

network and holographic Rényi entropy, *Journal of High Energy Physics* **2017**, 10.1007/jhep11(2017)148 (2017).

[35] R. J. Harris, N. A. McMahon, G. K. Brennen, and T. M. Stace, Calderbank-Shor-Steane holographic quantum error-correcting codes, *Physical Review A* **98**, 10.1103/physreva.98.052301 (2018).

[36] A. Jahn, M. Gluza, F. Pastawski, and J. Eisert, Majorana dimers and holographic quantum error-correcting codes, *Physical Review Research* **1**, 10.1103/physrevresearch.1.033079 (2019).

[37] L.-Y. Hung, W. Li, and C. M. Melby-Thompson, p -adic CFT is a holographic tensor network (2019), arXiv:1902.01411 [hep-th].

[38] T. J. Osborne and D. E. Stiegemann, Dynamics for holographic codes, *Journal of High Energy Physics* **2020**, 10.1007/jhep04(2020)154 (2020).

[39] E. Gesteau and M. J. Kang, The infinite-dimensional happy code: entanglement wedge reconstruction and dynamics (2020), arXiv:2005.05971 [hep-th].

[40] C. Cao and B. Lackey, Approximate Bacon-Shor code and holography, *Journal of High Energy Physics* **2021**, 10.1007/jhep05(2021)127 (2021).

[41] A. Jahn, Z. Zimborás, and J. Eisert, Tensor network models of AdS/qCFT, *Quantum* **6**, 643 (2022).

[42] C. Cao, J. Pollack, and Y. Wang, Hyperinvariant multiscale entanglement renormalization ansatz: Approximate holographic error correction codes with power-law correlations, *Physical Review D* **105**, 10.1103/physrevd.105.026018 (2022).

[43] N. Bao, L.-Y. Hung, Y. Jiang, and Z. Liu, QG from SymQRG: $\text{AdS}_3/\text{CFT}_2$ correspondence as topological symmetry-preserving quantum RG flow (2025), arXiv:2412.12045 [hep-th].

[44] A. Jahn and J. Eisert, Holographic tensor network models and quantum error correction: a topical review, *Quantum Science and Technology* **6**, 033002 (2021).

[45] N. C. Menicucci, P. Van Loock, M. Gu, C. Weedbrook, T. C. Ralph, and M. A. Nielsen, Universal quantum computation with continuous-variable cluster states, *Physical Review Letters* **97**, 110501 (2006).

[46] J. I. Kwon, A. J. Brady, and V. V. Albert, Most continuous-variable cluster states are too entangled to be useless (2025), arXiv:2503.15698 [quant-ph].

[47] A. S. Holevo, M. Sohma, and O. Hirota, Capacity of quantum Gaussian channels, *Physical Review A* **59**, 1820 (1999).

[48] J. Eisert, M. Cramer, and M. B. Plenio, Colloquium: Area laws for the entanglement entropy, *Reviews of Modern Physics* **82**, 277 (2010).

[49] C. Weedbrook, S. Pirandola, R. García-Patrón, N. J. Cerf, T. C. Ralph, J. H. Shapiro, and S. Lloyd, Gaussian quantum information, *Reviews of Modern Physics* **84**, 621 (2012).

[50] See Supplemental Material for additional details and supporting derivations.

[51] G. Giedke and J. I. Cirac, Characterization of Gaussian operations and distillation of Gaussian states, *Physical Review A* **66**, 032316 (2002).

[52] G. Vidal, Class of quantum many-body states that can be efficiently simulated, *Physical Review Letters* **101**, 10.1103/physrevlett.101.110501 (2008).

[53] P. Calabrese and J. Cardy, Entanglement entropy and quantum field theory, *Journal of Statistical Mechanics: Theory and Experiment* **2004**, P06002 (2004), arXiv:hep-th/0405152 [hep-th].

[54] P. Calabrese and J. Cardy, Entanglement entropy and conformal field theory, *Journal of Physics A: Mathematical and Theoretical* **42**, 504005 (2009).

[55] J. Maldacena, Eternal black holes in anti-de Sitter, *Journal of High Energy Physics* **2003**, 021 (2003).

[56] M. Bañados, C. Teitelboim, and J. Zanelli, Black hole in three-dimensional spacetime, *Physical Review Letters* **69**, 1849 (1992).

[57] S. Xu and B. Swingle, Scrambling dynamics and out-of-time-ordered correlators in quantum many-body systems, *PRX Quantum* **5**, 10.1103/prxquantum.5.010201 (2024).

[58] M. Tajik, I. Kukuljan, S. Sotiriadis, B. Rauer, T. Schweigler, F. Cataldini, J. Sabino, F. Møller, P. Schüttelkopf, S.-C. Ji, *et al.*, Verification of the area law of mutual information in a quantum field simulator, *Nature Physics* **19**, 1022 (2023).

[59] M. Chen, N. C. Menicucci, and O. Pfister, Experimental realization of multipartite entanglement of 60 modes of a quantum optical frequency comb, *Physical Review Letters* **112**, 120505 (2014).

[60] W. Asavanant, Y. Shiozawa, S. Yokoyama, B. Charoensombutamon, H. Emura, R. N. Alexander, S. Takeda, J.-i. Yoshikawa, N. C. Menicucci, H. Yonezawa, *et al.*, Generation of time-domain-multiplexed two-dimensional cluster state, *Science* **366**, 373 (2019).

[61] M. V. Larsen, X. Guo, C. R. Breum, J. S. Neergaard-Nielsen, and U. L. Andersen, Deterministic multi-mode gates on a scalable photonic quantum computing platform, *Nature Physics* **17**, 1018 (2021).

[62] E. S. Cooper, P. Kunkel, A. Periwal, and M. Schleier-Smith, Graph states of atomic ensembles engineered by photon-mediated entanglement, *Nature Physics* **20**, 770 (2024).

[63] A. J. Kollár, M. Fitzpatrick, and A. A. Houck, Hyperbolic lattices in circuit quantum electrodynamics, *Nature* **571**, 45 (2019).

[64] D. Bluvstein, H. Levine, G. Semeghini, T. T. Wang, S. Ebadi, M. Kalinowski, A. Keesling, N. Maskara, H. Pichler, M. Greiner, *et al.*, A quantum processor based on coherent transport of entangled atom arrays, *Nature* **604**, 451 (2022).

[65] Q. Miao, T. Wang, K. R. Brown, T. Barthel, and M. Cetina, Probing entanglement scaling across a quantum phase transition on a quantum computer (2024), arXiv:2412.18602 [quant-ph].

[66] M. Iqbal, N. Tantivasadakarn, T. M. Gatterman, J. A. Gerber, K. Gilmore, D. Gresh, A. Hankin, N. Hewitt, C. V. Horst, M. Matheny, *et al.*, Topological order from measurements and feed-forward on a trapped ion quantum computer, *Communications Physics* **7**, 205 (2024).

[67] N. P. Breuckmann and B. M. Terhal, Constructions and noise threshold of hyperbolic surface codes, *IEEE Transactions on Information Theory* **62**, 3731 (2016).

[68] C. Cao, G. Cheng, A. Hamma, L. Leone, W. Munizzi, and S. F. E. Oliviero, Gravitational back-reaction is magical (2025), arXiv:2403.07056 [hep-th].

[69] N. Engelhardt and A. C. Wall, Quantum Extremal Surfaces: Holographic Entanglement Entropy beyond the Classical Regime, *Journal of High Energy Physics* **01**, 073 (2015), arXiv:1408.3203 [hep-th].

[70] N. Bao, S. Nezami, H. Ooguri, B. Stoica, J. Sully, and M. Walter, The holographic entropy cone, *Journal of High Energy Physics* **2015**, 10.1007/jhep09(2015)130

(2015).

[71] C. Cao, X.-L. Qi, B. Swingle, and E. Tang, Building bulk geometry from the tensor Radon transform, *Journal of High Energy Physics* **2020**, 10.1007/jhep12(2020)033 (2020).

[72] S. Baiguera, V. Balasubramanian, P. Caputa, S. Chapman, J. Haferkamp, M. P. Heller, and N. Y. Halpern, Quantum complexity in gravity, quantum field theory, and quantum information science, *Physics Reports* **1159**, 1 (2026).

[73] J. Magan, M. Sasieta, and B. Swingle, Random circuits in the black hole interior, *SciPost Physics* **19**, 10.21468/scipostphys.19.1.007 (2025).

[74] G. Vidal, Entanglement renormalization, *Physical Review Letters* **99**, 220405 (2007).

[75] T. F. Demarie, Pedagogical introduction to the entropy of entanglement for Gaussian states, *European Journal of Physics* **39**, 035302 (2018).

[76] J. Williamson, On the algebraic problem concerning the normal forms of linear dynamical systems, *American Journal of Mathematics* **58**, 141 (1936).

[77] M. M. Wolf, F. Verstraete, M. B. Hastings, and J. I. Cirac, Area laws in quantum systems: Mutual information and correlations, *Physical Review Letters* **100**, 070502 (2008), arXiv:0704.3906 [quant-ph].

Supplementary Information for “Building Holographic Entanglement by Measurement”

In this supplement we expand upon the background theory and constructions used for the quench-and-measure protocol in the main text. In Sec. I we review the continuous geometries that we will discretize with graph constructions. In Sec. II we motivate the graphs we use for discretizations. In Sec. III, we present additional numerical data showing how correlations and entanglement entropies depend on the graph parameters and the specific construction (undecorated vs. decorated) chosen, and compare correlations to mutual information. Finally, in Sec. IV we provide a self-contained review of the calculation of entanglement properties of Gaussian states from the covariance matrix.

I. REVIEW OF $(2+1)$ D GEOMETRIES APPEARING IN $\text{AdS}_3/\text{CFT}_2$

In the main text we consider two classes of geometries to demonstrate the quench-and-measure protocol. The first of these is the hyperbolic disk, which we think of as a spatial slice of AdS_3 . The second is the wormhole geometry, which we think of as the spatial slice of two-sided BTZ black hole geometry. In AdS/CFT , the first of these geometries would correspond to the ground state of the dual CFT. The second would correspond to a thermal state of the CFT. Here we review these geometries and show how the RT surfaces referenced in the main text may be obtained.

The key technical fact is that all the geometries of interest can be presented using an embedding space approach. We embed each $(2+1)$ D geometry into a $(2+2)$ D space with coordinates (T_1, T_2, X_1, X_2) and metric

$$ds_4^2 = -dT_1^2 - dT_2^2 + dX_1^2 + dX_2^2. \quad (\text{S.1})$$

This is a flat spacetime with two time-like and two space-like directions. The embedding takes the form of a hyperboloid

$$-T_1^2 - T_2^2 + X_1^2 + X_2^2 = -\ell_{\text{AdS}}^2. \quad (\text{S.2})$$

Here ℓ_{AdS} is the curvature radius also known as the AdS radius. This presentation is convenient because it gives a simple formula for the geodesic distance between two points in the $(2+1)$ D space. If P and Q are points on the hyperboloid, then the $(2+1)$ D distance obeys

$$\cosh \frac{d_{\text{bulk}}}{\ell_{\text{AdS}}} = -\frac{P \cdot Q}{\ell_{\text{AdS}}^2} \quad (\text{S.3})$$

where \cdot denotes the inner product in the $(2+2)$ D metric (S.1).

This framework is convenient for our purposes because, in AdS/CFT applied to a $(2+1)$ D bulk, the minimal surface that computes the entanglement reduces to a minimal curve, i.e. a geodesic. So by fixing the boundary region of interest using the points P and Q , we can read off the relevant geodesic lengths from (S.3). Then the entanglement entropy of the boundary region is obtained from the RT formula,

$$S = \frac{d_{\text{bulk}}}{4G}. \quad (\text{S.4})$$

The Brown-Henneaux relation for the central charge, $c = \frac{3\ell_{\text{AdS}}}{2G}$, allows us to convert from bulk units to the central charge characterizing the CFT. We also note that, as discussed in the main text, it is often necessary to perform an outer overall minimization over different candidate RT surfaces built from local geodesics.

1. AdS_3

We first discuss the case of AdS , which corresponds to the CFT ground state. The coordinates in $(2+1)$ D are (r, t, θ) and the embedding map is

$$\begin{aligned} T_1 &= \sqrt{\ell_{\text{AdS}}^2 + r^2} \sin \frac{t}{\ell_{\text{AdS}}}, & T_2 &= \sqrt{\ell_{\text{AdS}}^2 + r^2} \cos \frac{t}{\ell_{\text{AdS}}}, \\ X_1 &= r \cos \theta, & X_2 &= r \sin \theta, \end{aligned} \quad (\text{S.5})$$

which leads to the induced metric

$$ds_3^2 = - \left(1 + \frac{r^2}{\ell_{\text{AdS}}^2} \right) dt^2 + \frac{1}{1 + \frac{r^2}{\ell_{\text{AdS}}^2}} dr^2 + r^2 d\theta^2. \quad (\text{S.6})$$

Introduce a large r cutoff at $r = r_c$ and consider a cutoff-anchored geodesic from $(0, r_c, 0)$ to $(0, r_c, \Delta\theta)$. The corresponding $(2+2)$ D points are

$$\begin{aligned} P &= (0, \sqrt{\ell_{\text{AdS}}^2 + r_c^2}, r_c, 0), \\ Q &= (0, \sqrt{\ell_{\text{AdS}}^2 + r_c^2}, r_c \cos \Delta\theta, r_c \sin \Delta\theta). \end{aligned} \quad (\text{S.7})$$

Thus the distance obeys

$$\cosh \frac{d_{\text{bulk}}}{\ell_{\text{AdS}}} = 1 + \frac{r_c^2}{\ell_{\text{AdS}}^2} (1 - \cos \Delta\theta). \quad (\text{S.8})$$

Using the fact that the cutoff r_c is large, we obtain the simplified form

$$d_{\text{bulk}} \approx \ell_{\text{AdS}} \ln \left(4 \frac{r_c^2}{\ell_{\text{AdS}}^2} \sin^2 \frac{\Delta\theta}{2} \right). \quad (\text{S.9})$$

The entropy is

$$S = \frac{d_{\text{bulk}}}{4G} = \frac{\ell_{\text{AdS}}}{2G} \ln \left(\frac{2r_c}{\ell_{\text{AdS}}} \sin \frac{\Delta\theta}{2} \right), \quad (\text{S.10})$$

or, using the Brown-Henneaux relation,

$$S = \frac{c}{3} \ln \left(\sin \frac{\Delta\theta}{2} \right) + (\text{constant}). \quad (\text{S.11})$$

This formula is invariant under the replacement $\Delta\theta \rightarrow 2\pi - \Delta\theta$ as required by the purity of the ground state.

2. BTZ Black Hole

We next discuss the case of the non-rotating BTZ black hole, which corresponds to a CFT thermal state. Specifically, we consider a two-sided black hole that corresponds to a purification of the mixed thermal state into a thermofield double state (TFD). The coordinates in $(2+1)$ D are again (r, t, θ) and the embedding map is

$$\begin{aligned} T_1 &= \frac{\ell_{\text{AdS}} \sqrt{r^2 - r_+^2}}{r_+} \sinh \frac{r_+ t}{\ell_{\text{AdS}}^2}, & T_2 &= \frac{\ell_{\text{AdS}} r}{r_+} \cosh \frac{r_+ \theta}{\ell_{\text{AdS}}}, \\ X_1 &= \frac{\ell_{\text{AdS}} \sqrt{r^2 - r_+^2}}{r_+} \cosh \frac{r_+ t}{\ell_{\text{AdS}}^2}, & X_2 &= \frac{\ell_{\text{AdS}} r}{r_+} \sinh \frac{r_+ \theta}{\ell_{\text{AdS}}}, \end{aligned} \quad (\text{S.12})$$

with r_+ a constant. The induced $(2+1)$ D metric is

$$ds_3^2 = - \frac{r^2 - r_+^2}{\ell_{\text{AdS}}^2} dt^2 + \frac{\ell_{\text{AdS}}^2}{r^2 - r_+^2} dr^2 + r^2 d\theta^2 \quad (\text{S.13})$$

which has a horizon at $r = r_+$. The location of the horizon fixes the thermodynamic properties of the solution, including its temperature

$$T = \frac{r_+}{2\pi\ell_{\text{AdS}}^2} \quad (\text{S.14})$$

and thermal entropy

$$S_{th} = \frac{2\pi r_+}{4G} = \frac{\pi^2 T \ell_{AdS}^2}{G} = \frac{2\pi^2 c \ell_{AdS} T}{3}. \quad (S.15)$$

One can identify the physical length of the circle on which the CFT lives with the proper distance at the cutoff surface,

$$L_{CFT} = 2\pi r_c. \quad (S.16)$$

Setting $x_{CFT} = r_c \theta$ and $t_{CFT} = \frac{r_c}{\ell} t$, the induced metric on the cutoff surface is

$$ds_{CFT}^2 = -dt_{CFT}^2 + dx_{CFT}^2. \quad (S.17)$$

In this time coordinate, the CFT temperature is

$$T_{CFT} = \frac{\ell_{AdS}}{r_c} T. \quad (S.18)$$

The thermal entropy is then

$$S_{th} = \frac{\pi c L_{CFT} T_{CFT}}{3}, \quad (S.19)$$

which is the standard formula for $(1+1)D$ CFT.

We now consider the one-sided and two-sided entropies, starting with the one-sided case. For the same cutoff anchored boundary points as in the AdS_3 case, the embedding space points are now

$$\begin{aligned} P &= (0, \frac{\ell_{AdS} r_c}{r_+}, \frac{\ell_{AdS} r_c}{r_+}, 0), \\ Q &= (0, \frac{\ell_{AdS} r_c}{r_+} \cosh \frac{r_+ \Delta \theta}{\ell_{AdS}}, \frac{\ell_{AdS} r_c}{r_+}, \frac{\ell_{AdS} r_c}{r_+} \sinh \frac{r_+ \Delta \theta}{\ell_{AdS}}). \end{aligned} \quad (S.20)$$

With the same large r_c simplification, the distance is

$$\exp \frac{d_{bulk}}{\ell_{AdS}} = \frac{4r_c^2}{r_+^2} \sinh^2 \frac{r_+ \Delta \theta}{2\ell_{AdS}}. \quad (S.21)$$

Taking this geodesic as a candidate for the RT surface, we get a candidate for the entropy,

$$S^{(1)} = \frac{d_{bulk}}{4G} = \frac{c}{3} \ln \left(\frac{2r_c}{r_+} \sinh \frac{r_+ \Delta \theta}{2\ell_{AdS}} \right). \quad (S.22)$$

An alternative geodesic is provided by the union of the horizon and the analog of the above geodesic but for the complementary boundary region. The corresponding entropy candidate is

$$S^{(2)} = S_{th} + \frac{c}{3} \ln \left(\frac{2r_c}{r_+} \sinh \frac{r_+ (2\pi - \Delta \theta)}{2\ell_{AdS}} \right). \quad (S.23)$$

The general formula for the one-sided entropy predicted by RT is thus

$$S = \min(S^{(1)}, S^{(2)}). \quad (S.24)$$

In the two-sided case, one candidate RT surface is a union of two one-sided surfaces, one for the boundary region in the left asymptotic region and one for the boundary region in the right asymptotic region. Another option is a surface that connects the boundary region end points in the left asymptotic region to the corresponding endpoints in the right asymptotic region. Each of these two geodesics is itself composed of a geodesic from $r = r_c$ to $r = r_+$ at constant t and θ . The points in this case are

$$\begin{aligned} P &= (0, \frac{\ell_{AdS} r_c}{r_+}, \frac{\ell_{AdS} r_c}{r_+}, 0), \\ Q &= (0, \ell_{AdS}, 0, 0). \end{aligned} \quad (S.25)$$

This partial distance obeys

$$\exp \frac{d'_{\text{bulk}}}{\ell_{\text{AdS}}} = \frac{2r_c}{r_+}, \quad (\text{S.26})$$

so the full distance is

$$d_{\text{bulk}} = 4d'_{\text{bulk}} = 4\ell_{\text{AdS}} \ln \frac{2r_c}{r_+}. \quad (\text{S.27})$$

We may obtain the same formula by identifying the second asymptotic region with $t \rightarrow t + i\beta/2$. The geodesic length from the left boundary endpoint $(0, r_c, 0)$ to the right boundary endpoint $(i\beta/2, r_c, 0)$ can be found from the points

$$\begin{aligned} P &= (0, \frac{\ell_{\text{AdS}} r_c}{r_+}, \frac{\ell_{\text{AdS}} r_c}{r_+}, 0), \\ Q &= (0, \frac{\ell_{\text{AdS}} r_c}{r_+}, -\frac{\ell_{\text{AdS}} r_c}{r_+}, 0). \end{aligned} \quad (\text{S.28})$$

The corresponding distance obeys

$$\exp \frac{d''_{\text{bulk}}}{\ell_{\text{AdS}}} = 4 \frac{r_c^2}{r_+^2}, \quad (\text{S.29})$$

and the full distance is now twice d''_{bulk} giving again $d_{\text{bulk}} = 4\ell_{\text{AdS}} \ln \frac{2r_c}{r_+}$.

The corresponding candidate two-sided entropy is

$$S^{(\text{two-sided, alt})} = \frac{2c}{3} \ln \frac{2r_c}{r_+}. \quad (\text{S.30})$$

Comparing to $2S^{(1)}$ from the one-sided calculation, these two surfaces exchange relevance when $\Delta\theta$ satisfies

$$\sinh \frac{r_+ \Delta\theta}{2\ell_{\text{AdS}}} = 1, \quad (\text{S.31})$$

which is the condition used to estimate the location of the crossover between the two entanglement entropy curves in Fig. 2(c) of the main text. Note that this calculation assumes no interior to the wormhole; if there is an interior then the two-sided alternate lengths will be longer and hence the transition to the plateau will occur at larger interval size.

II. DISCRETIZING BULK GEOMETRIES WITH GRAPHS

Our protocol requires the discretization of a spatial slice of a continuous bulk geometry into a representative graph. The chosen graph should approximate the bulk geometry in the following sense: if each node in the graph is identified with a position in the bulk, edges should only exist between nodes nearby in proper distance. All edges in the graph should have approximately the same associated proper distance, which justifies use of an unweighted graph to represent the spatial slice of the bulk geometry.

1. Discretizing the hyperbolic disk: MERA graph

To discretize the hyperbolic disk, we use a graph G inspired by the MERA tensor network [26, 74]. This graph is formed by combining a tree graph of branching ratio $b = 2$ with additional edges that connect the nodes within each level of the tree into a ring, as shown in Fig. 1(a) of the main text. For a tree of total depth R_b , the boundary has $L = 2^{R_b}$ nodes, while the bulk has $N_{\text{bulk}} = 2^{R_b} - 1$ nodes, yielding in total $N_{\text{bulk}} + L = 2^{R_b+1} - 1$ nodes.

We can now associate each bulk node with an approximate position inside the continuous geometry of the AdS_3 spatial slice. We consider $r \gg \ell_{\text{AdS}}$ and define

$$d\mathbf{z} = \ell_{\text{AdS}} \frac{dr}{r}. \quad (\text{S.32})$$

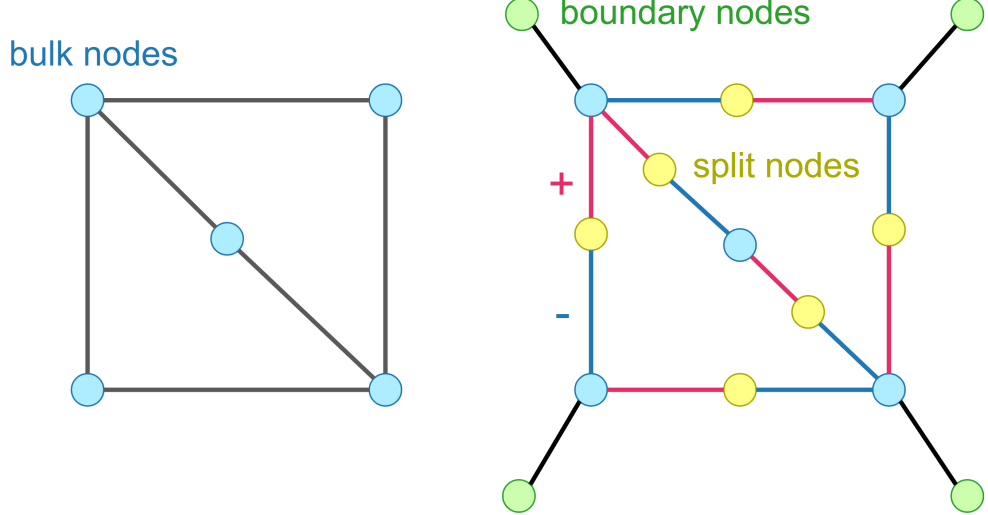


FIG. S1. An illustration of the decoration construction. **Left:** The initial bulk graph (blue nodes) used to form the decorated graph. In this example, the outermost four sites are chosen to be adjacent to the boundary. **Right:** The added boundary nodes (green) are connected to the pre-selected adjacent bulk nodes. All bulk-to-bulk edges are also divided with split nodes (yellow), with the adjacent pair of links assigned + or - in the coupling matrix.

With the constraint that the proper distance between adjacent levels of the tree should equal the proper distance between adjacent nodes within a level of 2^R nodes at depth R , we find

$$r = \frac{\ell_{\text{AdS}} \ln 2}{2\pi} e^{\varepsilon/\ell_{\text{AdS}}} \quad (\text{S.33})$$

such that the approximate spatial metric can be written as

$$ds^2 = d\varepsilon^2 + \left(\frac{\ell_{\text{AdS}} \ln 2}{2\pi} \right)^2 e^{2\varepsilon/\ell_{\text{AdS}}} d\theta^2. \quad (\text{S.34})$$

Here $d_{\text{adj}} = \ell_{\text{AdS}} \ln 2$ is the approximate proper distance between adjacent nodes. In these coordinates, bulk nodes in a layer of depth R are placed at $\varepsilon = R d_{\text{adj}}$ and are spaced within a layer by $\Delta\theta = 2\pi/L = 2\pi/2^n$.

2. Discretizing the wormhole

As discussed in Sec. I, by ‘‘wormhole’’ geometry we refer to the spatial slice of the two-sided BTZ black hole. For large r , the one-sided BTZ metric approaches AdS_3 . To form the two-sided BTZ solution, two one-sided BTZ geometries are glued together at r_+ . This suggests that as an approximation one can discretize the two-sided BTZ solution by gluing together two graphs that each approximate a large- r region of AdS_3 .

To accomplish this, we take two copies of the hyperbolic disk graph, and remove nodes with depth less than some integer R_+ . The nodes at depth R_+ in each graph can either be identified (in the case of no wormhole interior) or connected through a cylindrical mesh to represent the wormhole interior. In Fig. 2(c) in the main text, we show the case where an edge is drawn between each node at depth R_+ and equal angular position in the two copies of the hyperbolic disk graph.

3. Decoration

Decoration, which is illustrated in Fig. S1, is a procedure that alters the graph used to discretize a spatial geometry. Take a graph $G = (V, E)$ with vertices V and unweighted edges E . In this case, all of the original vertices should be thought of as bulk vertices. Given G and a subset $V_O \subset V$, we define a decorated graph $G_D = (V_D, E_D)$ with vertices

V_D and weighted edges E_D in the following manner. First, we subdivide the graph, splitting each edge $e \in E$ into two edges $e^+ \in E^+$ and $e^- \in E^-$ by inserting vertices. These inserted vertices, which we call ‘‘split’’ nodes, form the subset $V_S \subset V_D$. Edges in E^+ have weight +1 and edges in E^- have weight -1. Finally, for every vertex $v_O \in V_O$, a boundary vertex $v_{\text{bdy}} \in V_{\text{bdy}}$ is added to the graph and connected to v_O via an edge with weight +1. The vertex set of G_D is thus

$$V_D = V \cup V_S \cup V_{\text{bdy}} \quad (\text{S.35})$$

and it contains $|V| + |E| + |V_{\text{bdy}}|$ vertices in total. The edge set E_D contains two edges for each original edge, from the splitting procedure, and a new edge for each boundary vertex. It contains $2|E| + |V_{\text{bdy}}|$ edges in total.

The quench Hamiltonian associated with the decorated graph G_D follows its (weighted) adjacency matrix A_D . The quench Hamiltonian has the form

$$H_q = \frac{1}{2} \sum_{\langle ij \rangle \in E_D} J_{ij} x_i x_j, \quad (\text{S.36})$$

where $J_{ij} = A_{D,ij}$. During the measurement process of the quench-and-measure protocol, both V and V_S are measured.

The decorated graph yields much cleaner power laws of correlations than the undecorated case, because contributions to the covariance from different paths starting and ending on the same boundary anchors constructively add, as described in the main text. The decorated construction was also motivated by attempts to embed the Laplacian $L = D - A$ of a graph G into the covariance matrix produced after the quench. The appearance of the Laplacian in the post-quench, pre-measurement covariance matrix of the decorated procedure can be noted by examining A_D^2 , which appears in the momentum-momentum block of the covariance matrix (cf. Eq. (5) of the main text). The values of A_D^2 are a weighted sum of length-2 paths, such that due to the form of decoration, the Laplacian L of the original graph contributes to the bulk node block of A_D^2 . We were motivated to engineer the appearance of the bulk Laplacian because of a basic element of the AdS/CFT dictionary which relates a boundary operator of scaling dimension Δ to a bulk field of mass $m_{\text{cont}} \sim \Delta/\ell_{\text{AdS}}$. We speculated that scale-invariant correlations could be obtained by mimicking the appearance of a massive free field in the bulk. Since the lattice Hamiltonian of a continuum massive free field of mass m_{cont} is set by $L + m_{\text{cont}}^2$, the Laplacian was a natural target. In practice, calculations showed that decoration produces cleaner entanglement entropy whose fit central charge saturates to near $c = 1$ at strong squeezing. This is suggestive of a free scalar CFT on the boundary, however, the presence of additional terms in the covariance matrix complicates this identification.

III. CORRELATIONS AND ENTANGLEMENT IN THE HYPERBOLIC DISK GEOMETRY

Our protocol for engineering holographic entanglement includes several tuning knobs: how strongly we squeeze the initial state, how finely we discretize the target bulk geometry in converting it to a graph, and whether or not we decorate the graph. This section presents supplemental numerical data examining the dependence of correlations and entanglement on these parameters for the hyperbolic disk geometry. We comment on implications for prospective experimental implementations and for the theoretical interpretation of our construction.

1. Entanglement entropies

While deep graphs are theoretically appealing for approaching the limit of a smooth geometry, smaller graphs offer the most convenient starting point for experimental implementations. Thus, in Fig. S2(a) we examine how the entanglement entropy S depends on the size of the graph for depths $R_b = 3, 4, 5$ at fixed initial squeezing $\mu = 0.1$ in both the undecorated (top) and decorated (bottom) constructions. Additionally, in Fig. S2(b), we plot the entanglement entropy at fixed depth $R_b = 5$ for different values of the initial squeezing μ . In each case, the dependence of entanglement entropy S on region size ℓ is well described by a fit with the functional form of the CFT prediction

$$S_{\text{gs}}(\ell) = \frac{c}{3} \ln \left(\sin \frac{\Delta\theta}{2} \right) + \epsilon, \quad (\text{S.37})$$

where $\Delta\theta = 2\pi\ell/L$.

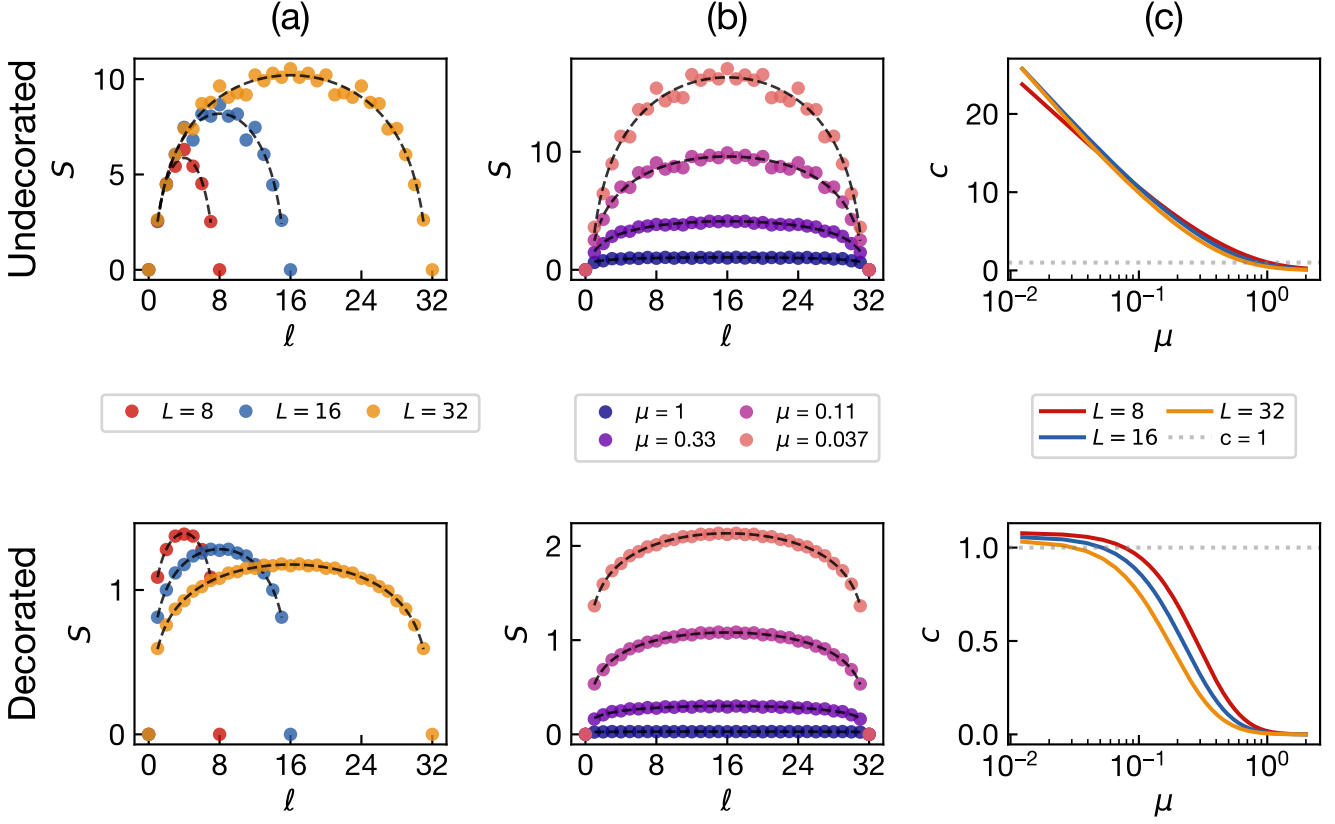


FIG. S2. Comparison of results for different graph sizes and squeezing values for both the undecorated and decorated cases. The columns show (a) entanglement entropy for various boundary sizes (corresponding to depths of 3 through 5) with a fixed squeezing $\mu = 0.1$, (b) entanglement entropy for various μ for fixed depth of 5, (c) fit central charge as a function of squeezing. For the entanglement entropy plots fits to the (1+1)D CFT entanglement entropy curve are shown in dashed black lines. In the decorated case, in the limit of small μ the fit central charge c approaches an approximate value of 1.

From each fit to the entanglement entropy, we extract a central charge c . In the undecorated case, we find that the central charge increases logarithmically with the inverse squeezing parameter, $c \propto \log(1/\mu)$, in the regime of strong squeezing $\mu \ll 1$. By contrast, in the decorated case, the central charge approaches a saturation value $c \approx 1$ in the limit of strong squeezing $\mu \ll 1$. Intriguingly, the saturation value $c \approx 1$ coincides with the prediction for a 1+1-dimensional free boson CFT.

While the limit of strong initial squeezing is a theoretically simple case, in which quenching on the bulk couplings produces an ideal graph state, in practice experiments operate at finite squeezing and may contend with tradeoffs between the degree of squeezing and the complexity of control over the coupling graph. Thus, the good agreement of the entanglement entropy with the CFT model regardless of initial squeezing — and down to small system sizes — offers convenience for near-term experimental implementations.

2. Correlations and Mutual Information

A major motivation for the decorated graph is that it produces correlations of uniform sign, allowing us to observe a clean power-law decay. By contrast, analyzing the correlations in the undecorated case is complicated by their non-uniform sign. However, a convenient proxy is to examine the mutual information $I(i:j)$ between pairs of sites i, j , which sets an upper bound on the correlations

$$\text{Corr}(\phi_i, \phi_j) = \frac{\text{Cov}(\phi_i, \phi_j)}{\sqrt{(\text{Var}\phi_i)(\text{Var}\phi_j)}} \leq \sqrt{2I(i:j)}, \quad (\text{S.38})$$

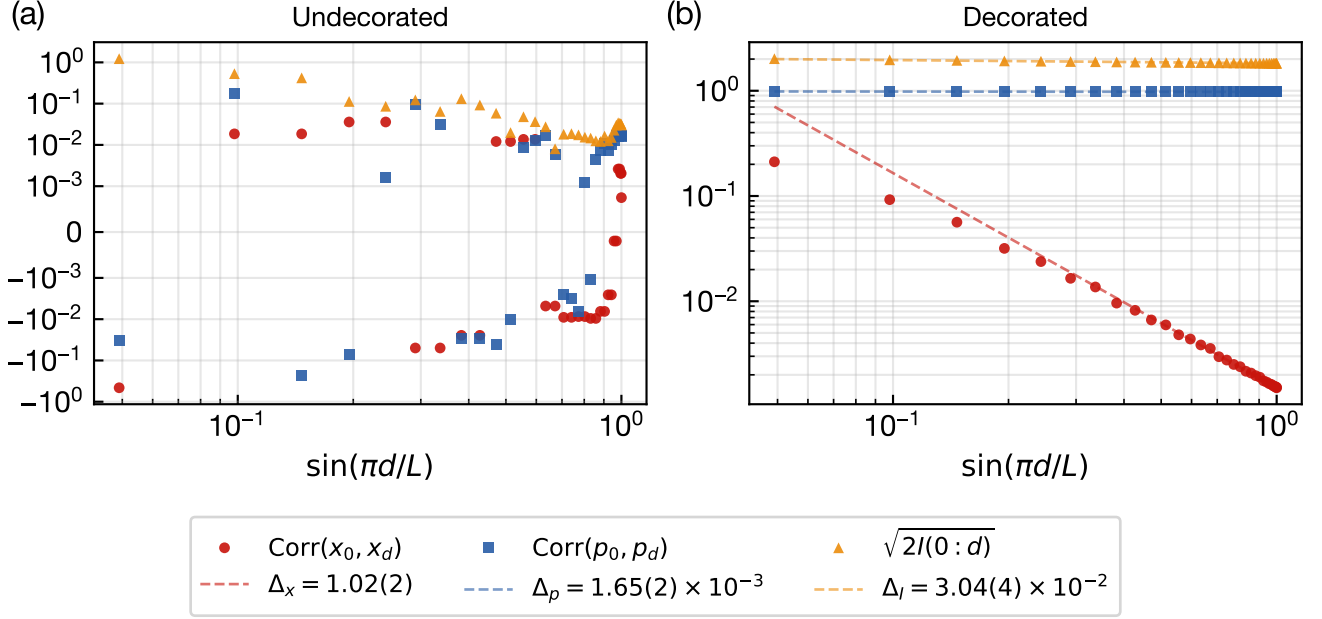


FIG. S3. Correlations and mutual information in the (a) undecorated and (b) decorated case. For both cases, a graph with depth $R_b = 6$ is used with squeezing $\mu = 0.01$. For the decorated case, power law fits (dashed lines) yield the respective scaling dimensions Δ shown in the legend. The least-squares fits are performed over the third of the points with the largest $\sin(\pi d/L)$, and the uncertainties shown are standard errors.

where $\phi \in \{x, p\}$ is a quadrature operator. The calculation of the mutual information and its role as a bound on covariances are reviewed in Sec. IV 2.

We analyze correlations and mutual information obtained from the quench-and-measure protocol on the MERA graph in Fig. S3, which shows both the undecorated and decorated cases. For both the undecorated and decorated cases, $\sqrt{2I(i:j)}$ indeed bounds both x and p correlations. Additionally, in the decorated case, power law behavior emerges at large $\sin(\pi d/L)$, where $d = |i - j|$ is the distance on the boundary separating the two nodes. We fit the correlations as a power law $\text{Corr}(\phi_0, \phi_d) \propto d^{-2\Delta_\phi}$ with the scaling dimension Δ_ϕ for each operator ϕ as a free parameter. The corresponding exponent Δ_I for mutual information is fit by $I(\phi_0 : \phi_d) \propto d^{-2\Delta_I}$. These scaling dimensions depend on the squeezing μ , as shown in Fig. S4. In particular, for small μ , the scaling dimension Δ_x approaches 1. The domains for the fits are over the third of the data with the largest $\sin(\pi d/L)$.

IV. CORRELATIONS, ENTANGLEMENT, AND MUTUAL INFORMATION OF GAUSSIAN STATES

1. Calculating Entanglement Entropies from the Covariance Matrix

The entanglement structure of a Gaussian state is fully determined by the covariance matrix. In the main text, after deriving the covariance matrix of the state prepared by the quench-and-measure protocol, we use it to determine the entanglement entropy $S = -\text{Tr}(\rho_A \log \rho_A)$ of a boundary subregion A with density matrix ρ_A . More generally, we evaluate Rényi entropies

$$S_\alpha = \frac{1}{1 - \alpha} \log \text{Tr}(\rho_A^\alpha), \quad (\text{S.39})$$

where the entanglement entropy is obtained in the limit $S = \lim_{\alpha \rightarrow 1} S_\alpha$. The calculation of entanglement entropy from covariances of Gaussian states was derived in Ref. [47] and is presented in several review articles [48, 49, 75]. We nevertheless here provide a brief self-contained derivation aimed at providing physical intuition.

A foundation for our analysis is that any Gaussian state can be related by a *symplectic transformation* to a product state whose entropy will be straightforward to calculate. A symplectic transformation is one that preserves

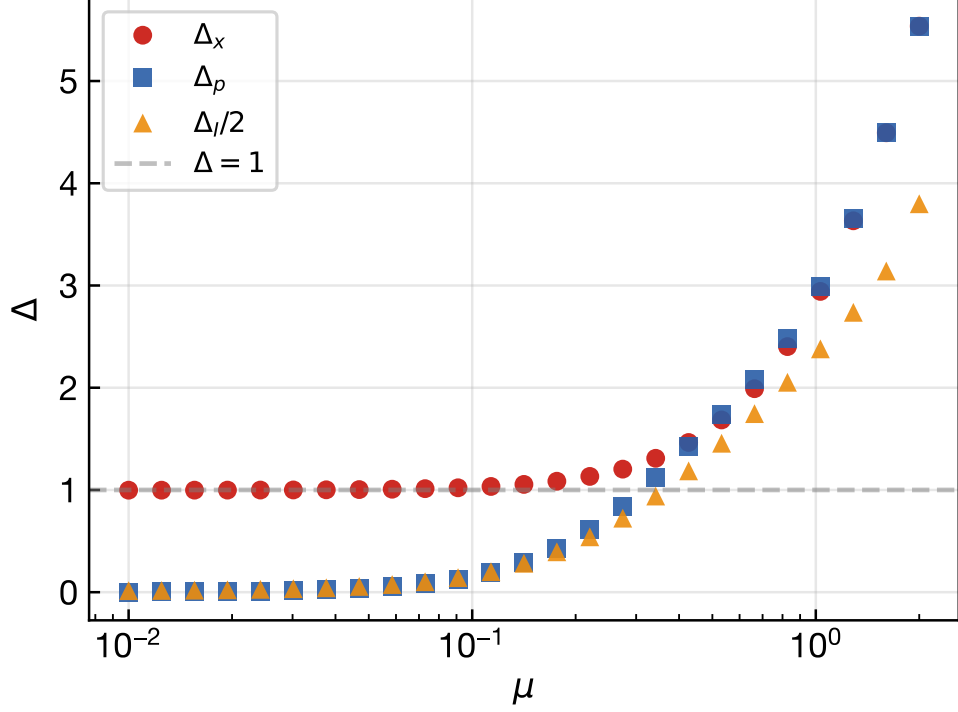


FIG. S4. Scaling dimensions Δ for x , p , and mutual information I as a function of squeezing μ for a decorated graph of depth $R_b = 6$.

the commutation relations, and correspondingly also preserves the phase space volume and entropy. By Williamson's theorem [76], there exists such a transformation \mathcal{S} that converts the covariance matrix \mathcal{V}_A to diagonal form: $\mathcal{S}\mathcal{V}_A\mathcal{S}^T = D = \text{diag}(\nu_1, \nu_1, \nu_2, \nu_2, \dots, \nu_M, \nu_M)$ for any M -mode Gaussian state. In other words, \mathcal{S} transforms to a basis of collective modes, in terms of which the system A is in an unsqueezed product state $\rho_A = \otimes_m \rho_m$. The *symplectic eigenvalues* ν_m represent the variances $\langle X_m^2 \rangle = \langle P_m^2 \rangle = \nu_m$ of quadrature operators in each collective mode indexed m , which is thus precisely in a thermal state with mean occupation $\langle n \rangle_m = \frac{1}{2} \langle X_m^2 + P_m^2 \rangle - \frac{1}{2} = \nu_m - \frac{1}{2}$, where the subtraction of $1/2$ accounts for zero-point fluctuations.

We now use the statistical mechanics of the quantum harmonic oscillator to determine the entropy $S = -\langle \log \rho \rangle$ of each collective mode. In particular, for a single mode in a thermal state of inverse temperature β , for which the mean occupation number is $\langle n \rangle = 1/(e^\beta - 1)$, the entropy is given by

$$S = (\langle n \rangle + 1) \log(\langle n \rangle + 1) - \langle n \rangle \log \langle n \rangle. \quad (\text{S.40})$$

Expressing the occupation $\langle n_m \rangle = \nu_m - \frac{1}{2}$ of each eigenmode in terms of its symplectic eigenvalue ν_m and summing over modes, we arrive at the entanglement entropy

$$S = \sum_m \left[\left(\nu_m + \frac{1}{2} \right) \log \left(\nu_m + \frac{1}{2} \right) - \left(\nu_m - \frac{1}{2} \right) \log \left(\nu_m - \frac{1}{2} \right) \right]. \quad (\text{S.41})$$

Note that Eq. S.41 correctly yields an entropy proportional to the logarithm of the phase space volume in the classical limit, since $S \approx \sum_m (\log \nu_m + 1)$ when $\nu_m \gg 1$ for all modes.

The Rényi entropies defined in Eq. S.39 are analogously determined by first evaluating $\text{Tr}(\rho^\alpha)$ for a thermal state ρ of a harmonic oscillator. In terms of the mean occupation $\langle n \rangle$, we obtain

$$\text{Tr}(\rho^\alpha) = \frac{1}{(\langle n \rangle + 1)^\alpha - \langle n \rangle^\alpha}. \quad (\text{S.42})$$

Substituting this result into Eq. S.39 and summing over modes with symplectic eigenvalues $\nu_m = \langle n \rangle_m + \frac{1}{2}$ yields

Rényi entropies

$$S_\alpha = \frac{1}{\alpha - 1} \sum_m \log \left[\left(\nu_m + \frac{1}{2} \right)^\alpha - \left(\nu_m - \frac{1}{2} \right)^\alpha \right]. \quad (\text{S.43})$$

To make use of the above entropy formulas, we require a prescription for determining the symplectic eigenvalues from the correlation matrix. Recall that the symplectic transformation \mathcal{S} , by definition, preserves the commutation relations $\Omega_{ij} = i[\xi_i, \xi_j]$. Here, $\xi = (x_1, p_1, \dots, x_M, p_M)$ is the vector of local quadrature operators, such that $\Omega = \bigoplus_{j=1}^M \Omega_j$ is the direct sum of matrices

$$\Omega_j = \begin{pmatrix} 0 & -1 \\ 1 & 0 \end{pmatrix} \quad (\text{S.44})$$

specifying the commutation relations for each oscillator indexed j . Formally, then, a symplectic transformation is one that satisfies $\mathcal{S}\Omega\mathcal{S}^T = \Omega$. From this symplectic identity, it can be shown that the diagonal matrix $\tilde{\Omega} \equiv \Omega D$ has the same eigenvalues as $\tilde{\mathcal{V}}_A \equiv \Omega\mathcal{V}_A$. In particular, both of these matrices have $2M$ eigenvalues $\lambda_{m\pm} = \pm i\nu_m$. Thus, finding the positive eigenvalues of $i\mathcal{V}_A = i\Omega\mathcal{V}_A$ by standard matrix diagonalization yields the symplectic eigenvalues ν_m of the covariance matrix \mathcal{V}_A .

We apply this symplectic diagonalization to covariance matrices \mathcal{V}_A of various subregions A to calculate the entanglement entropies (Eq. S.41) and Rényi entropies (Eq. S.43) plotted in the main text. The entropies thus calculated also allow us to determine mutual information $I(A : B) = S_A + S_B - S_{AB}$ between pairs of subsystems A and B .

2. Mutual Information as a Bound on Correlations

We also comment that the mutual information bounds correlations of the oscillators. For bounded operators O_A and O_B supported on regions A and B , there is a standard bound [77] on their covariance

$$\text{Cov}(O_A, O_B) = \langle O_A O_B \rangle - \langle O_A \rangle \langle O_B \rangle, \quad (\text{S.45})$$

of the form

$$\text{Cov}(O_A, O_B)^2 \leq 2I(A : B) \|O_A\|^2 \|O_B\|^2. \quad (\text{S.46})$$

Position and momentum operators are unbounded, so this does not directly apply to them.

For a pair of commuting variables which have a joint Gaussian probability distribution, ξ_A and ξ_B , there is a well known classical bound

$$\frac{\text{Cov}(\xi_A, \xi_B)^2}{\text{Var}(\xi_A)\text{Var}(\xi_B)} \leq 1 - e^{-2I}. \quad (\text{S.47})$$

This follows by direct computation of the terms involved. Since ξ_A and ξ_B automatically commute if A and B are disjoint regions in the system, this classical bound suffices for bounding correlations between different regions of the boundary.

It is also true that $1 - e^{-2I} \leq 2I$ for $I \geq 0$. They have identical values and first derivatives at $I = 0$, and the second derivative of $1 - e^{-2I}$ is less than zero. Thus $1 - e^{-2I}$ grows more slowly than $2I$ and we also get the bound

$$\frac{\text{Cov}(\xi_A, \xi_B)^2}{\text{Var}(\xi_A)\text{Var}(\xi_B)} \leq 2I. \quad (\text{S.48})$$

This is analogous to the general bound with the square of the operator norm replaced by the variance of the Gaussian variables.